

Insights into α B-crystallin polydispersity from native microfluidic high-field electrophoresis measurements

Maya A. Wright,^{†,□}, Francesco Simone Ruggeri,[†] Kadi L. Saar,[†], Pavan K. Challa,[†] Justin L. P. Benesch,[‡] and Tuomas P. J. Knowles^{*,†,¶}

[†]Department of Chemistry, University of Cambridge, Lensfield Road, CB2 1EW

□ Fluidic Analytics Ltd., Unit 5 Chesterton Mill, French's Road CB4 3NP

[‡]Department of Physical and Theoretical Chemistry, University of Oxford

[¶]Department of Physics, University of Cambridge, JJ Thomson Ave, Cambridge CB3 0HE

E-mail: tpjk2@cam.ac.uk

Abstract

In recent years, significant advancements have been made in the understanding of the population distributions and dynamic oligomeric states of the molecular chaperone α B-crystallin and its core domain variants. In this work, we provide solution-phase evidence of the polydispersity of α B-crystallin using microfluidic methods, used for separating the oligomeric species present in solution according to their different electrophoretic mobilities on-chip in a matter of seconds. We, in particular demonstrate that microfluidic high-field electrophoresis and diffusion can detect the oligomerisation of these highly dynamic molecular chaperones and characterise the dominant oligomeric species present. We thereby provide a robust microfluidic method for characterising the individual species within complex protein mixtures of biological relevance.

Introduction

α B-crystallin (α BC), a member of the small heat shock protein family, is one of the most important molecular chaperones that combat protein misfolding and the formation of aggregates under conditions of cell stress¹⁻³. α BC has a range of pathological interaction partners including that of α -synuclein, insulin and A β ⁴⁻⁸, and as such plays a key role in maintaining protein homeostasis within human cells. In addition to such important functions,⁹ α BC has been the target of biophysical studies in particular because of its self-assembly behaviour under physiological conditions. α BC typically exists as a distribution of oligomers, with sizes ranging from 10-mers to 40-mers (**Figure 1a**)¹⁰⁻¹². In addition, the various quaternary structures of α BC exist in a state of dynamic equilibrium, such that the subunits of α BC are able to exchange readily through rapid attachment or detachment of monomers to clusters¹³. The polydispersity and dynamic nature of α BC therefore presents significant difficulties in elucidating the oligomeric distributions of α BC in the solution phase under native conditions without the interference of a surface or a matrix.

Despite the many challenges present, advancements have been made in probing the nature and mechanisms of α BC self-assembly^{12,14-20}. Monomeric α BC is known to consist of a C-terminal domain, which is a chain of approximately 10 amino acid residues, an α -crystallin core domain, and an N-terminal extension^{13,21,22}. Oligomeric α BC consists of a dimeric sub-structure, where heterodimers form through overlap of the core domains on adjacent α BC molecules through intra-dimer contacts^{12,16-20}, as shown in **Figure 1b**. Assembly of these dimeric substructures into higher order oligomers is mediated through inter-dimer interactions of the flexible C-terminal extensions with the α -crystallin core domains on adjacent oligomers¹⁷, resulting in an overall polyhedral oligomer architecture (**Figure 1c**)¹³. Despite the significant advancements in understanding the oligomerisation of α B-crystallin, there currently do not exist solution-phase biophysical techniques that have high enough resolution and short enough measurement timescales below that of the subunit exchange timescales of α BC which can be used to probe the populations of α BC oligomers under native-like conditions.

Here, to address this problem, we utilised microfluidic high-field electrophoresis and diffusion techniques to probe α BC oligomerisation, and to quantify the physical parameters associated with the variety of oligomers present in the highly heterogeneous system. We first validated the separation technique by deconvolving a binary mixture of proteins of known hydrodynamic radii. We then progressed to characterise the individual oligomeric components within α BC in combination with spectroscopic analysis techniques to provide a method of detecting

polydispersity in the solution phase. We in addition probed the average oligomerisation properties of a variety of core domain variants of α BC, and found that microfluidic diffusion and electrophoresis measurements give insights into their propensity to oligomerise under native conditions.

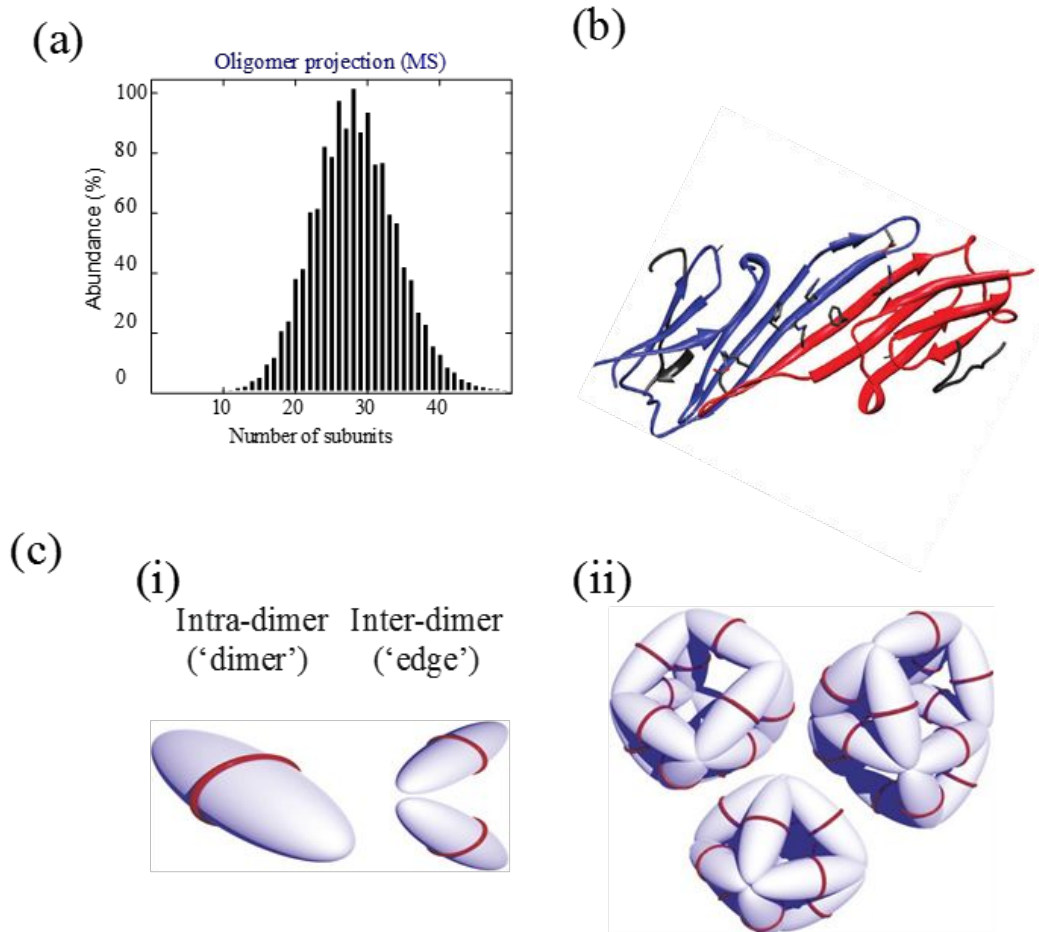


Figure 1. (a) Oligomeric population distribution of α BC obtained by quantitative mass spectrometry measurements. Reproduced from¹³. (b) Dimeric substructure of α B-crystallin, formed through the overlap of adjacent α -crystallin core domains. Reproduced from¹⁴. (c) Modes of interaction between α BC molecules. (i) Intra-dimer interactions hold two α BC molecules together, and inter-dimer interactions link adjacent dimeric subunits. (ii) The result is an overall polyhedral α BC architecture. Reproduced from ref⁹.

Results and Discussion

Microfluidic high-field electrophoresis

In this work, we utilised microfluidic high-field electrophoresis to separate protein species according to their electrophoretic mobilities.²³ The principle behind high-field electrophoresis involves applying a voltage across an electrophoresis chamber to deflect analyte molecules in proportion to their charge to hydrodynamic radius ratios. The voltage is applied via electrolyte solution (3 M of KCl) flanking the sides of the electrophoresis chamber, which form the electrodes (**Figure 2**).

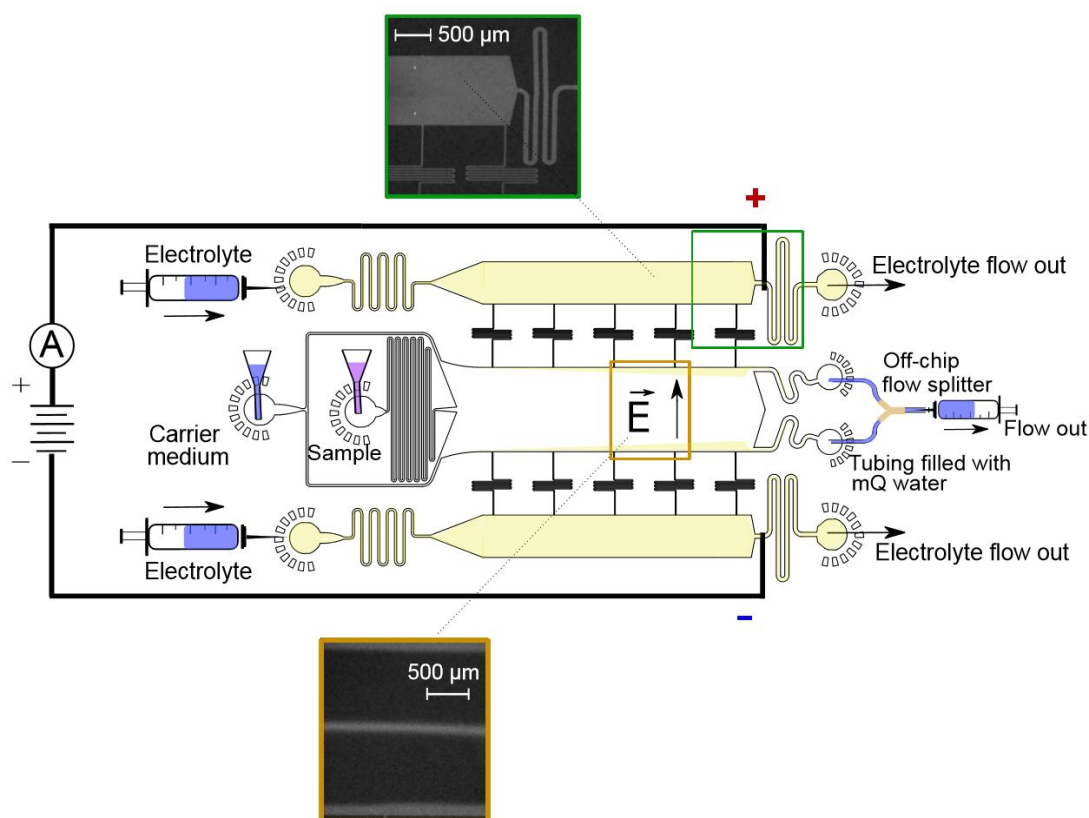


Figure 2. The high-field electrophoresis device. Schematic of the device. Electrolyte solution (yellow) is infused into the device via syringes and pumps, while sample and carrier medium stored in gel loading tips are introduced by withdrawing from the outlets using a flow splitter. A voltage is applied at the outlets and is carried into the device via the electrolyte solution (yellow), resulting in an electric field being applied across the main channel. Deflection of the analyte is imaged at the position highlighted by the orange square. The image in the orange square corresponds to BSA at 1 mg/mL. The image in the green square is a close up the electrolyte channels filled with 3M KCl plus BSA 2mg/mL for visualisation.

In particular, this configuration allows any electrolysis products formed at the interface between the metal electrodes and solution, i.e. at the device outlets, to be carried into the waste collection tubes

1
2
3 in the direction of flow.²⁴ This ensures steady flow within the electrophoresis chambers without any
4 disruption from the formation of gaseous electrolysis products, and allows high voltages to be applied
5 across the device for observation of maximum sample deflection.
6
7

8 We imaged the sample deflection at various applied voltages using an intrinsic fluorescence
9 microscope, which allows direct excitation of the aromatic amino acid residues within protein
10 sequences, and in particular of tryptophan (W) and tyrosine (Y) amino acids.²⁴ Therefore, all proteins
11 were observed in their native states, in solution and without any interference from a covalently
12 attached fluorophore. We analysed the data as previously described to calculate the electrophoretic
13 mobilities of the protein samples.²³
14
15
16
17
18
19

20 **Separation of binary protein mixtures in high-field devices**

21

22 We first proceeded to separate a binary protein mixture comprised of β -lactoglobulin (β -lac,
23 $M_w = 18.4$ kDa, $pI = 4.93$) and thyroglobulin (Tg, $M_w = 669$ kDa, $pI = 5.40$) in Tris and phosphate
24 buffers at pH values between 6.3 and 8 using the microfluidic high-field electrophoresis devices.
25
26

27 First, we determined the individual mobilities of each protein at pH 8, pH 7 and pH 6.3 in
28 order to quantify the effect of pH on the mobilities of the individual components, and to explore the
29 conditions necessary for achieving separation. The concentrations used were 160 μ M for β -lac and
30 12 μ M for thyroglobulin at pH 8 and pH 7 and 330 μ M for β -lac and 12 μ M for thyroglobulin at pH
31 6.3. The concentrations were adjusted for the different content of aromatic amino acid residues
32 fluorescent at the detection wavelength, and also to achieve clear peak separation at different pH. The
33 measurements were repeated in triplicates at each pH, using a separately fabricated microfluidic
34 device or under a different flow rate.
35
36
37
38
39
40

41 The electrophoretic mobilities of β -lac and Tg at each pH were calculated from the slope of
42 the best fit line for the plot of the migration velocity vs the electric field. We found that the
43 electrophoretic mobilities of β -lac and Tg depend strongly on pH, as shown in **Figure 3a**. At pH 6.3,
44 β -lac and Tg have a 33 % difference in their electrophoretic mobility values, while at pH 8, their
45 relative difference decreases to 5%. Since electrophoretic mobility is proportional to the ratio between
46 the charge q and the radius r , q/r , and the radii of the two proteins remain constant as a function of
47 pH, the difference in their mobilities is a result of the different solvated charges of the two proteins.
48 This is likely to be due to the difference in the two proteins' amino acid sequences and the 3D
49 structures, which dictate the degree of burying of their ionised residues. This result led us to compare
50 quantitatively the solvated charges of the two proteins in solution and the values of the predicted vs
51
52
53
54
55
56
57
58
59
60

measured charges, which are summarised in **Figure 3b-c**. Solvated charges were calculated based on equation 3 (Materials and Methods), and predicted charges were determined using the ExPASy bioinformatics tool.²⁵ The hydrodynamic radii of β -lac and Tg used were 2.34 and 8.50 nm respectively, which were determined by microfluidic diffusion measurements and from the literature^{26,27}. We found that the solvated charge decreases as the pH is lowered, as is the case with the predicted charge sequences. In addition, the solvated charges are lower compared to that of the predicted charge sequences. This is likely owing to the fact that predicted sequence charges are calculated solely based on the pKa of ionisable groups in the protein amino acid sequence and do not take into account protein structure or folding.^{28,29} Therefore, it is likely that in the 3D protein structure, some of the ionised amino acid groups are buried within the protein's core, and that only a few of the charged groups remain on the surface, leading to a lower measured solvated charge relative to that of the predicted charge. In fact, depending upon the pH, our results indicate that the ratio of the predicted to solvated charge of a protein can vary between 20 and 300%, and therefore, assuming a predicted charge based on sequence may not always be a true indication of the protein state in solution.

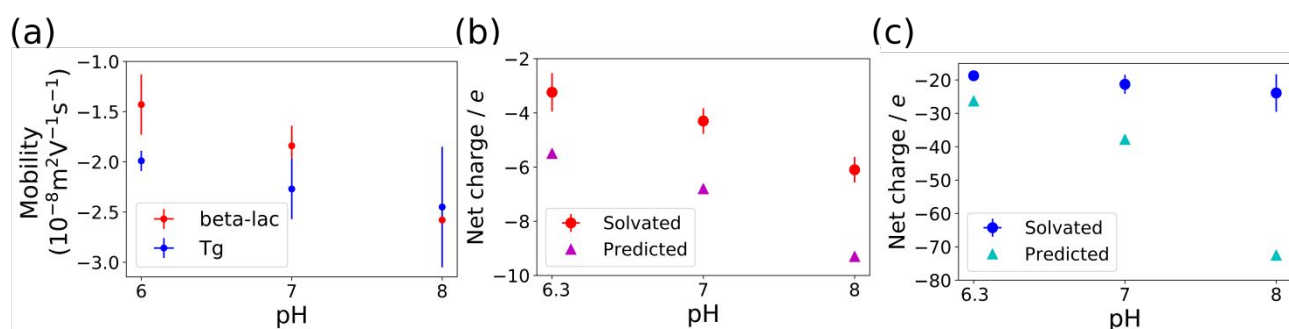


Figure 3. Electrophoretic mobilities and net charges of β -lac and Tg. (a) Comparison of the electrophoretic mobilities of β -lac and Tg at pH 6.3, 7 and 8. (b) Comparison of the net solvated and net predicted charges based on the sequence of β -lac. (c) Comparison of the net solvated and net predicted charges based on the sequence of Tg.

With a clear view on the relative mobilities of β -lac and Tg at various pH values, we next proceeded to separate binary mixtures of these proteins on-chip under applied electric fields. We found a marked difference in the separation power of the two proteins at pH 7 and pH 6.3, and found that at pH 6.3, complete separation of the full-width at half-maximum could be achieved at high voltages (**Figure 4a,b**). However, at low voltages the mixture of the two proteins appeared as a single convoluted peak. Thus, we applied second derivative analysis to de-convolve the peaks at lower voltages and track the spatial evolution of the individual peaks corresponding to each protein as a function of applied voltage. As routinely applied in spectroscopic data, second derivative analysis

enables a fine resolving power to determine the position of convoluted peaks with different amplitude and width.³⁰⁻³⁶ In addition, mathematically, the amplitude of each peak in the second derivative is directly proportional to the height of each convoluted peak in the profile, while the amplitude of the second derivative peak is smaller for a broader peak within the electrophoretic profile. Using this method, we could already confirm the presence of the two protein components in the electrophoretic profile and their separation at pH 6.3 at effective applied voltages as low as 0.92 V, corresponding to an electric field of only 4.6 V/cm. (**Figure 4c**). As shown in **Figure 4d**, we were able to fit the electrophoretic profiles with each individual protein component in solution (chi-square < 10⁻⁶). To perform the convolution of the profile, we constrained the fit with the physical parameters imposed by the second derivatives analysis, such as the number of peaks, their positions and relative widths. For each of the two proteins, the area below the relative convoluted peak is correlated to the concentration of protein in solution. We can approximate the area *A* of each peak as proportional to the number of protein in solution $\#_{\text{protein}}$ and to the total number $\#_{W+Y}$ of intrinsic fluorescent tryptophan (W) and tyrosine (Y) amino acids within each protein, thus $A_{\text{peak}} \propto \#_{W+Y} \cdot \#_{\text{protein}}$. Since the number of intrinsic fluorescent amino acids in each protein sequence is different (β -lac W = 2 and Y = 9; Tg W = 41 and Y = 76), we considered the weighted total emission for each single protein in solution $\#_{(W+Y)} = W \cdot \epsilon_w(1000) + Y \cdot \epsilon_Y(150)$, where ϵ_w and ϵ_Y are the approximated intensities of tryptophan and tyrosine in our conditions. The ratio between the areas *A* below the peak of the β -lac and Tg is:

$$\frac{A_{\beta\text{-lac}}}{A_{\text{Tg}}} = \frac{\#_{(W+Y),\beta\text{-lac}} \cdot c_{\beta\text{-lac}}}{\#_{(W+Y),\text{Tg}} \cdot c_{\text{Tg}}} \quad (1)$$

The number of protein was easily determined by the relationship $\#_{\text{protein}} = c \cdot N_A$, where *c* is the concentration in solution and N_A the Avogadro number. From the fit, we calculated a ratio between the areas *A* below the peaks of the β -lac and Tg of $\frac{A_{\beta\text{-lac}}}{A_{\text{Tg}}} = 1.5 \pm 0.2$ (**Figure 4d**). From equation 1, follows that for the mixture of β -lac and Tg at pH 6.3 the relative concentration of β -lac and Tg is:

$$\frac{c_{\beta\text{-lac}}}{c_{\text{Tg}}} = \frac{A_{\beta\text{-lac}}}{A_{\text{Tg}}} \cdot \frac{\#_{(W+Y),\text{Tg}}}{\#_{(W+Y),\beta\text{-lac}}} = 30 \pm 3 \quad (2)$$

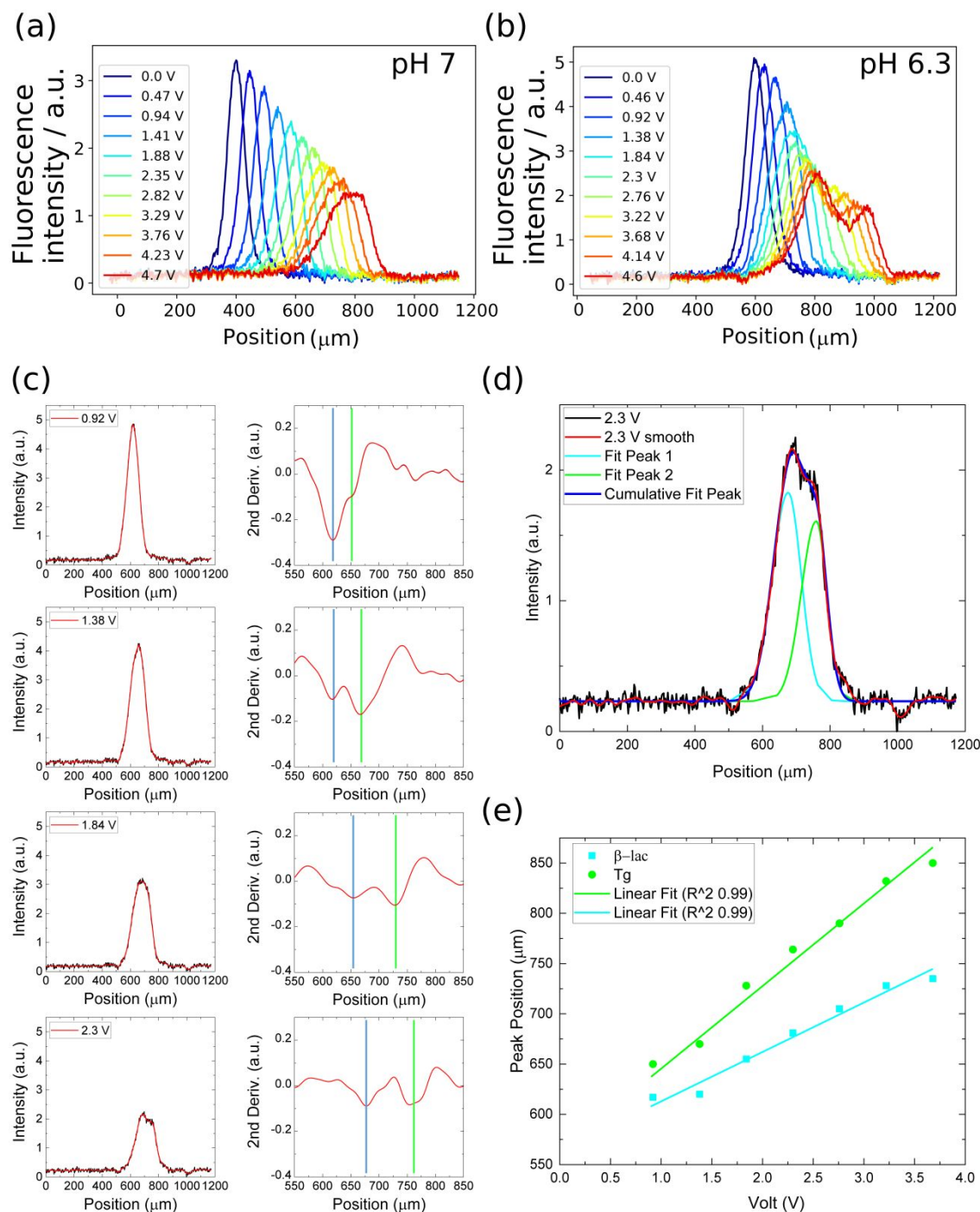


Figure 4. Separation of binary protein mixtures on-chip. (a) A mixture of β -lac (160 μM) and Tg (12 μM) at pH 7 was subjected to applied electric fields. However, separation could not be achieved at this pH due to their very similar electrophoretic mobilities under these conditions. (b) A mixture of β -lac (330 μM) and Tg (12 μM) at pH 6.3 could be separated much more clearly than at pH 7. (c) Second derivative analysis of the electrophoresis profiles of the β -lac and Tg mixture at pH 6.3. Left column: Shows data (black) and smoothed data using a Fourier transform and Savitzky-Golay filter (red) at four of the voltages. Right column: Second derivatives of the smoothed data. At 0.92 V, it is already possible to de-convolve the peaks relative to the two proteins. (d) Convolution fit of the electrophoretic profile at 2.3 V. (e) Peak position of the two proteins (blue for β -lac, black for Tg) plotted as a function of voltage drop across the channel. The lines correspond to the best fit to each set of data, and the slopes are used to calculate the electrophoretic mobilities.

1
2
3 The value obtained from the normalised ratio of the area of the peaks well corresponded with
4
5 the ratio between the used concentration of β -lac and Tg in solution, which was $\frac{C_{\beta-lac}}{C_{Tg}} = 28$ for the
6
7 mixture at pH 6.3. This result demonstrates that we could measure successfully the relative
8
9 concentration of a mixture of unknown samples, as well as to derive the values of intrinsic
10
11 fluorescence emission ϵ of a determined protein if its concentration is known.
12

13 Finally, by tracking the peak position of each protein as a function of voltage, we calculated
14
15 the electrophoretic mobilities of each component in the mixture in **Figure 3e**. We found $\mu_{\beta-lac} = -1.35$
16
17 $\cdot 10^{-8} \text{ m}^2 \cdot \text{V}^{-1} \cdot \text{s}^{-1}$ and $\mu_{Tg} = -2.25 \cdot 10^{-8} \text{ m}^2 \cdot \text{V}^{-1} \cdot \text{s}^{-1}$, which are values in good agreement with the
18
19 mobilities obtained for the individual components in **Figure 3a**. In contrast, at pH 7, we obtained a net
20
21 mobility of $\mu = 1.92 \pm 0.55 \cdot 10^{-8} \text{ m}^2 \cdot \text{V}^{-1} \cdot \text{s}^{-1}$, which corresponds to an averaged mobility of the two
22
23 components present in solution since this value lies between the individual measured mobilities of β -
24
25 lac and Tg at pH 7.
26

27 **Oligomerisation state of α B-crystallin variants**

28
29 Having established that we are able to separate with high resolution binary mixtures of protein using
30
31 our high-field electrophoresis set-up as well as determine the mobilities of the individual components,
32
33 we next proceeded to perform measurements on polydisperse samples of α B-crystallin variants. We
34
35 measured both the electrophoretic mobilities and hydrodynamic radii of WT α BC and a number of
36
37 truncated variants of the protein using microfluidic electrophoresis and diffusion.^{23,26} The variants
38
39 included the core domain of α BC with a single point mutation S135W for visualisation (α BC
40
41 S135W), which is known to exist in monomer-dimer equilibrium²⁰ with a low μM dissociation
42
43 constant K_d , and another small human heat shock protein that functions as the core domain of Hsp27
44
45 (cHsp27), a molecular chaperone with 54.7 % sequence similarity to α BC²⁰. In contrast to α BC
46
47 S135W, however, cHsp27 can be crosslinked to form an inter-dimer disulfide bond to prevent its
48
49 dissociation²⁰, and we were thereby able to measure cHsp27 in both its dimeric and dissociated forms
50
51 by controlling the crosslinking through the absence or presence of the reducing agent dithiothreitol
52
53 (DTT).

54 The electrophoresis and diffusion measurements were performed in 10 mM Tris buffer (pH
55
56 8) with Tween-20 surfactant (0.1% v/v) added to the co-flow buffer to inhibit adhesion of the proteins
57
58 to the PDMS, and at the following protein concentrations: WT α BC (157 μM), α BC S135W (230
59
60 μM and 292 μM), cHsp27 (212 μM) and cHsp27 (212 μM) with added excess DTT (1.8 mM). Each

protein measurement was repeated 2-4 times in separately fabricated devices or under different experimental flow rates. The results of the electrophoretic mobility and sizing measurements, as well as the corresponding calculated net solvated charges obtained, are summarised in **Figure 5b - d**, and **Table 1**.

Table 1: Summary of the physical parameters of α B-crystallin variants. Predicted charges were calculated using the ExPASy bioinformatics tool.²⁵

Protein	Mobility ($10^{-8} \text{ m}^2 \text{ V}^{-1} \text{ s}^{-1}$)	R_h (nm)	Charge (e)	Predicted monomer charge
WT α BC	-0.63 ± 0.13	6.59 ± 0.97	-4.88 ± 0.97	-1.3 (pH 8)
α BC S135W	-0.85 ± 0.2	1.79 ± 0.3	-1.79 ± 0.43	-1.4 (pH 8)
cHsp27 + DTT	-1.60 ± 0.1	1.42 ± 0.1	-2.67 ± 0.17	-3.7 (pH 8)
cHsp27	-2.11 ± 0.3	1.55 ± 0.1	-3.84 ± 0.6	-3.7 (pH 8)

The results are a convincing solution-phase demonstration that α BC exists in a highly oligomerised state. Both the hydrodynamic radius and measured net solvated charge of WT α BC indicate the presence of large clusters. The hydrodynamic radius of WT α BC is significantly higher than that of α BC S135W, which resembles α BC monomers and dimers, and the solvated charge of WT α BC is higher than that of its corresponding predicted monomer charge based on sequence alone using the ExPASy bioinformatics tool (**Figure 5c and d**).²⁵ In particular, the expected radius of WT α BC as a function of its molecular weight is of approximately 2 nm, while we observed a radius of 6.59 ± 0.97 nm. We can evaluate the number of monomers within a cluster considering the packing of n rigid spheres with diameter of 2 nm inside a sphere with radius of 6.59 ± 0.97 nm, with the closest possible packing of 0.74. Following this model, we calculated a number of monomers in the clusters $n = 23 \pm 7$, which well corresponds with what measured by mass spectrometry of 28 ± 10 (**Fig. 1**). The sequence charges are calculated for denatured proteins, with all ionised amino acid residues exposed to solvent. We found, however, in the previous section that net solvated charges of standard proteins such as β -lac and Tg are typically lower than that of their predicted counterparts due to the burying of ionised residues within the protein structure, which has been observed across a wide range of proteins.³⁷ Therefore, the fact that WT α BC, and indeed other constructs including α BC S135W and cHsp27, have a higher solvated charges than predicted is a strong indication of a

higher surface charge, and therefore the presence of oligomeric clusters in these proteins. This idea is further reinforced by comparing the solvated vs predicted charges of cHsp27 in the presence of DTT (**Figure 5c**). With DTT present, we would expect all of the disulfide bonds in cHsp27 to be reduced, and therefore that cHsp27 will be entirely monomeric. In contrast, in the absence of DTT, dimeric cHsp27 has a higher solvated than predicted charge, and it therefore appears that the relative values of the solvated vs predicted charges serves as an indication of oligomerisation. Overall, the hydrodynamic radii and net solvated charges obtained for WT α BC and its variants using microfluidic methods suggest oligomerisation behaviour that is in good agreement with reports from literature^{11-14,19,20}.

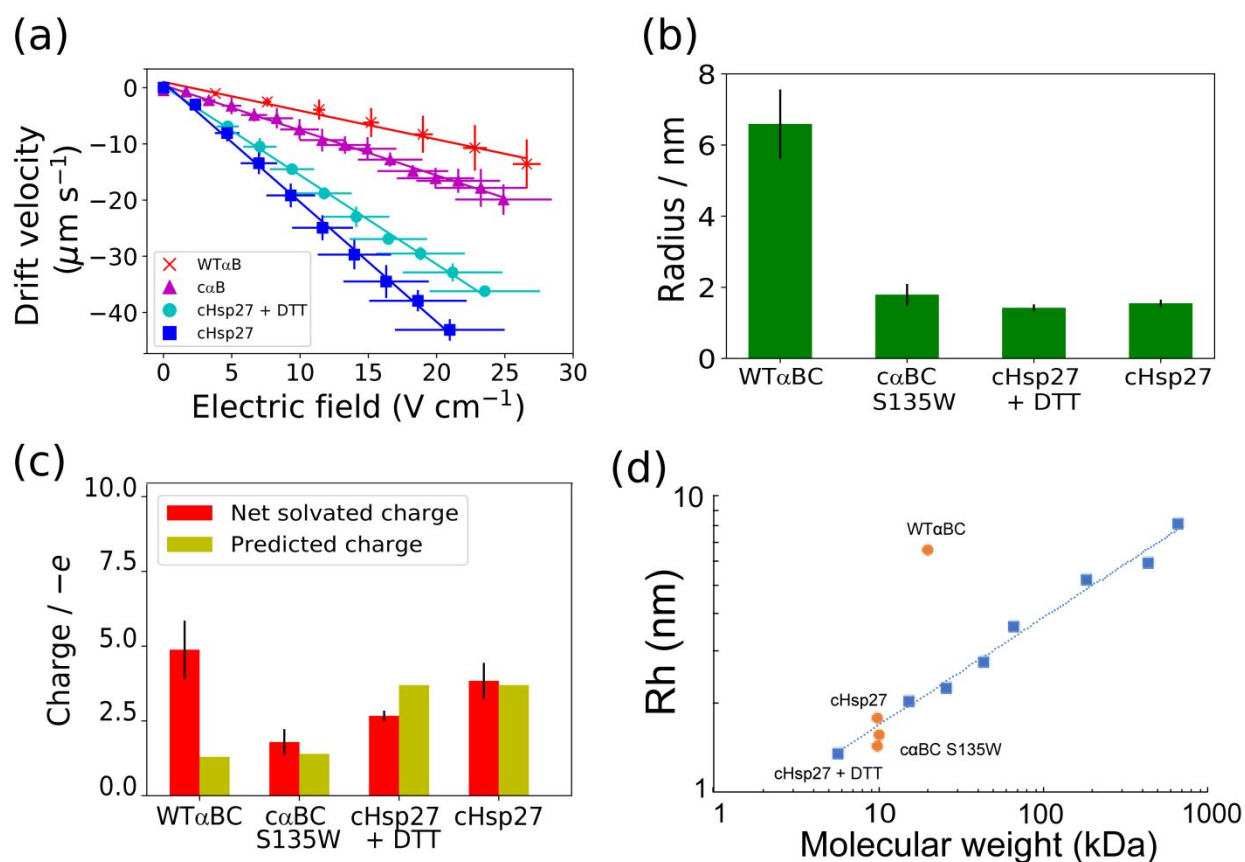


Figure 5. Summary of the physical properties of the α B-crystallin variants obtained. (a) Plot of drift velocity vs electric field for the four different α BC variants measured. Straight lines are the best fit to the data points, and the slopes of each line give the electrophoretic mobility of each sample. (b) Graph comparing the net solvated charge vs predicted monomeric charge of each α BC variant. Error bars show the standard deviation across replicates. Predicted charges were calculated using the ExpASY bioinformatics tool²⁵. (c) Graph comparing the hydrodynamic radii of each α BC variant. (d) Hydrodynamic radius (R_h) vs molecular weight for the different WT α BC variants, plus for several standard proteins (adapted from ³⁸).

Population distributions of α B-crystallin oligomers

We have demonstrated that the average physical properties of α BC and its truncated variants in the solution phase give insights into the oligomerisation state of each protein. We next sought to further quantify the oligomerisation by detecting the polydisperse distributions of the α BC constructs by analysing the microfluidic high-field electrophoresis data. In particular, building on the separation studies described in the previous section, we tested whether we could detect the presence of multiple protein oligomers species of different electrophoretic mobilities by analysing the fluorescence intensity profiles of the sample under applied electric fields by analysing their standard deviation and their second derivatives.

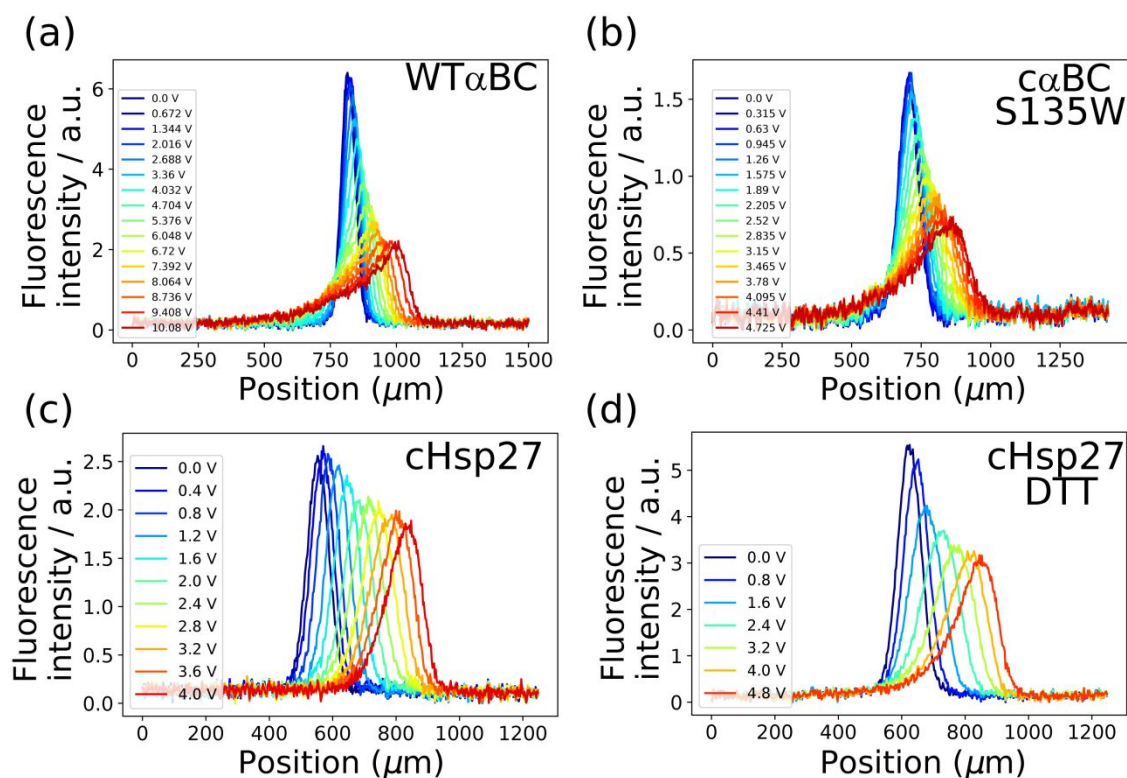


Figure 6. Fluorescence intensity profiles of WT α BC and its truncated variants under applied voltages. Effective voltage drops across the main channel are shown in the colour bar on the left. (a) WT α BC, withdrawal rate = 280 μ L/h, electrolyte infusion rate = 30 μ L/h. (b) c α BC S135W, withdrawal rate = 350 μ L/h, electrolyte infusion rate = 60 μ L/h. (c) cHsp27, withdrawal rate = 350 μ L/h, electrolyte infusion rate = 60 μ L/h. (d) cHsp27 + DTT, withdrawal rate = 350 μ L/h, electrolyte infusion rate = 60 μ L/h.

A comparison of the electrophoresis profiles of WT α BC, c α BC S135W, cHsp27 and cHsp27 with added DTT reveals that WT α BC and its truncated variants clearly differ in their oligomeric compositions. **Figure 6** shows the fluorescence scans of the four protein samples and corresponding effective voltage drops applied across the channel. We observed that the fluorescence intensity

1
2
3 profiles of WT α BC and α BC S135W exhibited significant asymmetry and spreading compared to
4 that of cHsp27 with and without DTT, which could be an indication of the presence of more than one
5 species. In WT α BC and α BC S135W, some species even deflect in the opposite direction, which
6 may in fact suggest the presence of residual protein species during protein purification that possess
7 positive charge. (**Figure 6a and b**).

8
9
10
11 We next proceeded to explore whether any information on the specific populations of
12 oligomeric species present could be obtained from the electrophoresis profiles of WT α BC. As such,
13 as with the binary mixture of proteins described earlier, we applied standard data analysis methods
14 used in spectroscopy to detect the presence of multiple convoluted peaks in the profiles of WT α BC,
15 thereby detecting the convoluted different oligomeric species present.^{39,40,35,41} The electrophoresis
16 profiles (Black lines, left of **Figure 7a-d**) were first smoothed using Fourier transform and Savitzky-
17 Golay filters (Red lines, left panels of **Figure 7a-d**). Next, the second derivative of the electrophoresis
18 profiles were calculated (right panels of **Figure 7a-d**). Each peak in the second derivative above the
19 background noise level signifies the presence of a convoluted peak within the electrophoretic profile.
20 The peaks in the second derivatives are associated to local regions with strong curvature (shoulders)
21 in the electrophoresis profiles, as shown by the green arrows in **Figure 7c-d**.

22
23
24
25
26
27
28
29
30
31 Analysing the WT α BC data obtained at different voltages revealed that at the three highest
32 effective voltages applied across the channel, we started to detect the presence of peaks in the second
33 derivative that lie above the noise level (two of them shown in **Figure 7c-d**). The peaks were present
34 at each voltage, increased in number and modified their position as a function of the increasing
35 voltage. This implies that the peaks are not an artefact of the background noise, but in fact are a result
36 of appearing of different oligomeric populations in the WT α BC electrophoresis profiles with
37 increasing voltage. Indeed we observed a higher number of shoulders in the profiles as a function of
38 increasing voltage (**Figure 7e**). As a further independent demonstration that the observed peaks are
39 related to the different mobilities of the several oligomeric families in solution, the total area of the
40 electrophoretic profiles as a function of the voltage is constant (**Figure 7f**), indicating that the profile
41 is only changing shape because of the presence of multiple oligomeric species with different
42 electrophoretic mobility. Furthermore, the same analysis on the monomeric-dimeric cHsp27 and
43 cHsp27 with added DTT showed the presence of a single peak till the highest voltage (**Figure SI 1**)
44 confirming that they are not significantly polydisperse compared to WT α BC, and that the peaks in
45 the WT α BC arose indeed from polydispersity.
46
47
48
49
50
51
52
53
54
55
56
57
58
59
60

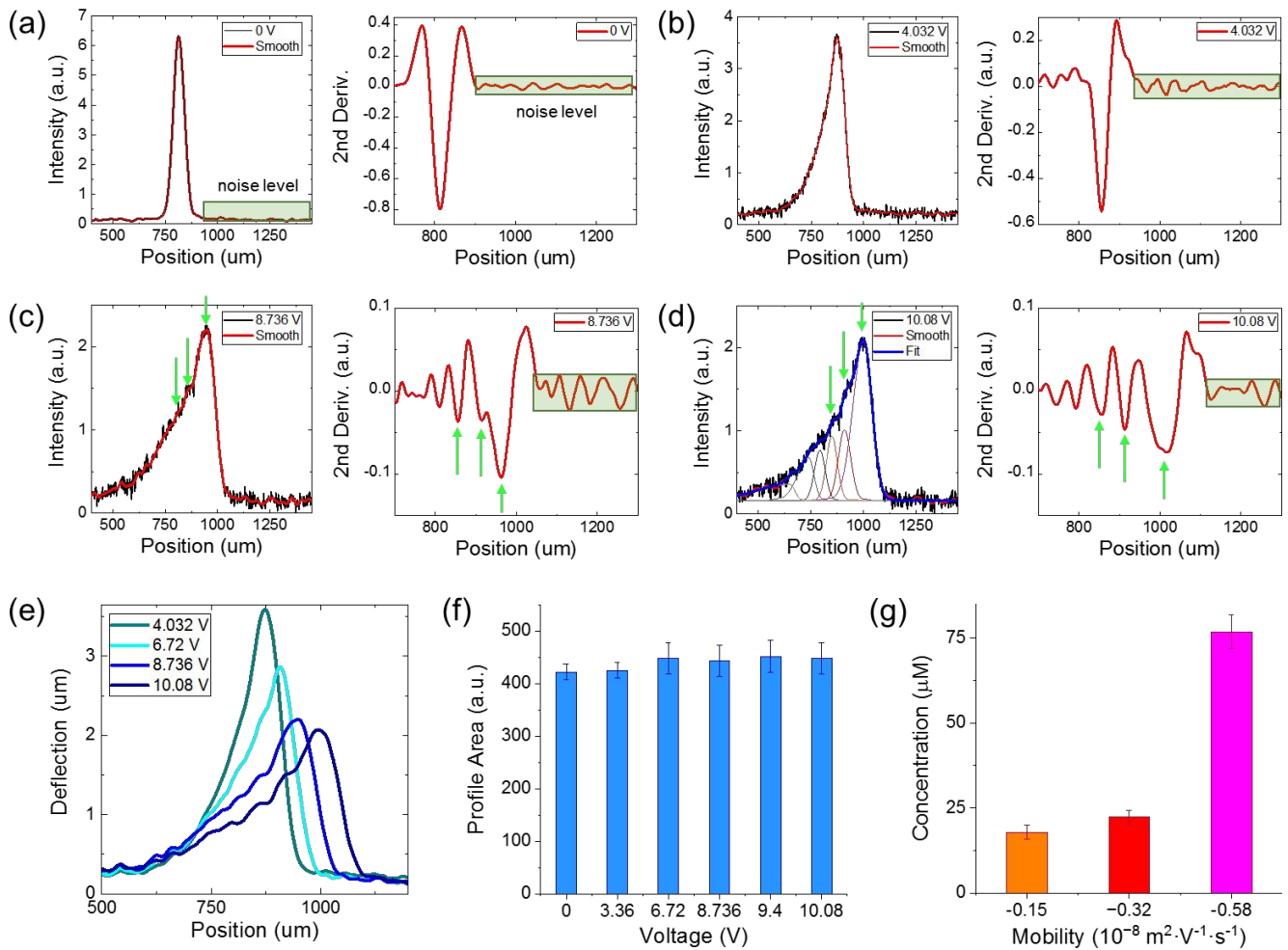


Figure 7. Second derivative analysis of α B-crystallin profiles at the three highest effective voltages. (left panels of a-d) The black and red lines show the raw data and the smoothed data after filtering, respectively. Green arrows denote the location of notable peaks in the profiles and second derivative. (right panels of a-d) The second derivative of the smoothed data is then taken, and analysed for the presence of peaks above the background noise level. We found the presence of peaks (shown by green arrows) that increase in magnitude with the effective voltage drop, implying increased separation of the oligomeric species at higher fields. (d) Convolution of the profile, we constrained the fit with the physical parameters imposed by the second derivatives, such as the number of peaks, their positions and relative widths. (e) The number of peaks in the second derivatives corresponds to shoulder in the profiles, which increase as a function of the voltage. (f) The area of the profiles is constant as a function of the voltage. (g) Absolute concentration vs mobility of each oligomeric species as calculated from equation 2.

In conclusion, we have observed the separation of the dominant oligomeric species within WT α BC polydisperse sample and that each convoluted peak could be associated to an oligomeric population with defined mobility. We could retrieve the mobility of each oligomeric species by tracking the positions of each deflected convoluted peak. At the highest applied voltage of 10.1 V, we could observe the presence of three convoluted peaks. We could identify the presence of three dominant oligomeric WT α BC species with negative mobilities of $-0.58 \cdot 10^{-8} \text{ m}^2 \cdot \text{V}^{-1} \cdot \text{s}^{-1}$, $-0.32 \cdot 10^{-8} \text{ m}^2 \cdot \text{V}^{-1} \cdot \text{s}^{-1}$

1
2
3 $^1 \cdot s^{-1}$ and $-0.15 \cdot 10^{-8} \text{ m}^2 \cdot \text{V}^{-1} \cdot s^{-1}$. Finally, considering **equation 2** in the case of a fixed number of
4 fluorescent amino acids $\#_{W+Y}$ for each species, that the area of the profile is constant and that the
5 sample of the WT α Bc a concentration of 157 μM , we could extrapolate the absolute concentration of
6 each oligomeric species in solution (**Figure 7g**).
7
8
9
10
11
12
13
14
15
16
17
18
19
20
21
22
23
24
25
26
27
28
29
30
31
32
33
34
35
36
37
38
39
40
41
42
43
44
45
46
47
48
49
50
51
52
53
54
55
56
57
58
59
60

Conclusions

In this work, we demonstrated the use of microfluidic diffusion, electrophoresis platforms and advanced spectroscopic analysis for probing firstly binary protein mixtures, and secondly the distributions of highly polydisperse biologically active protein clusters in free solution under native conditions. The protein assemblies were probed in their label-free native states using intrinsic fluorescence imaging. We performed native measurements on α B-crystallin oligomers and a variety of its monomeric and dimeric truncated variants, and found that we are able to detect protein self-assembly based on comparing the relative solvated charge of the clusters to their predicted charges based on sequence. We moreover found that the measured average hydrodynamic radii of the clusters provide further evidence of oligomerisation. In addition, we extracted information on mobility and the relative abundance of several co-existing oligomeric populations of α B-crystallin by combining microfluidic methods with spectroscopic analysis techniques on the obtained electrophoresis data. In particular, we de-convolve the profile by second derivative analysis of microfluidic fluorescence profiles demonstrating the presence of more than one species with different state of charge, and characterised the physical properties of each individual oligomeric components and quantified their concentrations. We thereby demonstrated the power of microfluidic methods, which provide solution-phase measurements of complex protein mixtures of biological interest under native conditions, in probing the dynamic and polydisperse nature of molecular chaperone systems.

Materials and Methods

Protein sample preparation

Buffers were prepared using chemicals from Sigma Aldrich, UK, and the proteins were prepared according to the following protocols. β -lactoglobulin, thyroglobulin and BSA were obtained from Sigma Aldrich as lyophilised powders and made up to the desired concentrations by weighing and diluting in buffer. Concentrations were checked using a NanoDrop spectrophotometer (Thermo Fischer Scientific) before each measurement. Full-length human α B-crystallin (α BC), core-domain α BC S135W (residues 68-153 with a point mutation) and core-domain Hsp27 (residues 84-176) were expressed and purified as previously described.²⁰ Where reduction of core-domain Hsp27 was required, a solution of dithiothreitol (DTT) stock solution was prepared in water and added to the core-domain Hsp27 samples at a molar ratio of 1:10 protein:DTT.

Microfluidic device fabrication

Microfluidic masks were first designed using AutoCAD, and the desired device geometry printed as a transparent blank onto an opaque thin film (Micro Lithography Services Ltd). Microfluidic devices were fabricated using soft-lithography.⁴² A layer of SU-8 photoresist (3 mL, MicroChemCorp) was spin-coated onto a silicon wafer (3 inch diameter, MicroChemicals) and baked at 96°C for 12 to 15 minutes. The height of the spin-coated layer was controlled to give the desired device height. SU8-3050 was used to produce 50 μ m devices. The photolithographic mask with the desired device geometry was placed on top of the coated silicon wafer, and clamped securely in position before exposure to UV light (40 s, 1000 mW)⁴³ to allow photochemical cross-linking of the irradiated portions of the photoresist. The silicon wafer was then post-baked for 5 minutes at 96°C and subsequently developed in PGMEA (Propylene glycol methyl ether acetate). The wafer was then rinsed in IPA (isopropanol) and dried with a nitrogen gun to yield a microfluidic master consisting of raised channels in the desired device geometry. The master was then cast in PDMS (polydimethylsiloxane). A 1:10 ratio of curing agent to PDMS elastomer (Dow Corning) was thoroughly mixed and poured onto the master in a petri dish. Carbon black nanopowder (Sigma Aldrich) was mixed thoroughly with the PDMS and the resultant mixture centrifuged for 5 minutes at 5000 rpm before pouring onto the microfluidic master. The petri dish was then placed in a desiccator for 30 min in order to remove air bubbles from the PDMS, and subsequently baked at 67°C for 150 min. The PDMS devices were then cut out with a scalpel and the inlets and outlets hole-

1
2
3 punched with 0.75 mm or 1.5 mm diameter biopsy punchers (World Precision Instruments). The
4 microfluidic devices were cleaned with IPA, thoroughly dried, and bonded to glass (Thermo
5 Scientific) or quartz (Alfa Aesar) microscope slides using an Electronic Diener Femto Plasma bonder
6 (30 s, 40 mW). The devices were then baked at 67°C for 30 min to ensure complete bonding to the
7 microscope slides. The bonded devices were then treated under oxygen plasma for 500 s at 80 mW
8 to ensure the channel surfaces became hydrophilic.⁴⁴ The oxygen plasma interacts with the surface
9 of the PDMS and induces radical formation.⁴⁵ The radicals then react with the plasma to form
10 functionalised groups containing oxygen at the surface, with hydrophilic properties. The channels
11 were then stored under water for up to a week until further use.
12
13
14
15
16
17
18

19 **High-field electrophoresis measurements**

20
21 After fabrication according to the procedure outlined in the previous section, microfluidic high field
22 electrophoresis devices were primed manually with milliQ water. Separately, two 1 mL plastic
23 syringes (Neolus Terumo) were filled with a mixture of 3 M KCl and trace amounts of BSA (2
24 mg/mL). Tracer molecules were included for visualisation of the electrolyte streams in the
25 microfluidic channels and chosen to fluoresce under the excitation wavelengths used in the sample
26 imaging. The electrolyte syringes were connected to a needle and polythene tubing (Fischer scientific,
27 inner diameter 0.86 mm, outer diameter 1.52 mm), and were interfaced with the electrolyte inlets of
28 the device using angled metal dispensing tips (Intertronics, 20 gauge, inner diameter 0.6 mm, 90°
29 angle). The two electrolyte outlets of the device (1.5 mm width) were then connected to electrodes,
30 consisting of angled metal dispensing tips (Intertronics, 15 gauge, inner diameter 1.25 mm, 90° angle)
31 soldered to silver wire, and connected to polythene tubing (Smiths Medical 800/100/500) for waste
32 collection. The microfluidic high field electrophoresis experiments were then performed.
33
34
35
36
37
38
39
40
41

42 Buffer and sample were inserted into their corresponding inlets on the device using gel-
43 loading tips. A 1 mL gastight glass syringe (Hamilton) and needle (Neolus Terumo, 20 gauge, 0.9 x
44 16 mm) were connected to a 3-way flow splitter (Elveflow) using polythene tubing (Fischer scientific,
45 inner diameter 0.86 mm, outer diameter 1.52 mm, length 10 cm). Two pieces of tubing were attached
46 to the outlets of the flow splitter and cut to 30 cm each. The syringe and flow splitter system were
47 filled with milliQ water, and the two free ends of tubing connected to angled metal dispensing tips
48 (Intertronics, 20 gauge, inner diameter 0.6 mm, 90° angle) which were subsequently inserted into the
49 device outlets. Flow through the system was controlled using nEMESYS syringe pumps (Centoni).
50 The two syringes filled with solutions of 3 M KCl were pushed such that electrolyte was infused into
51 the device, while fluid was simultaneously withdrawn through the device outlets connected to the
52
53
54
55
56
57
58
59
60

1
2
3 glass syringe. The flow rate utilised were either 60 $\mu\text{L}/\text{h}$ electrolyte infusion and 350 $\mu\text{L}/\text{h}$
4 withdrawal, or 50 $\mu\text{L}/\text{h}$ electrolyte infusion and 280 $\mu\text{L}/\text{h}$ withdrawal.
5
6

7 **Voltage application, imaging and data analysis**

8

9
10 Once fluid flow in the devices reached a steady state, a voltage scan was applied across the channels.
11 The electrode wires were connected to an external voltage supply and multimeter for simultaneous
12 voltage application and measurement of the current through the system. Typical voltage scans ranged
13 from the application of 0 V to 45 V in 5 V increments. At each voltage step, the analyte deflection
14 was imaged in triplicates at exposure times ranging from 500 to 5000 ms on an inverted fluorescence
15 microscope, attached to a CCD camera. Each voltage scan was repeated 3 times to ensure
16 reproducibility. After the sample measurement, each device was calibrated by filling the main
17 electrophoresis channel with solutions of 3 M KCl and repeating the voltage scan and current
18 measurements to estimate the effective voltage drops across the devices.²³
19
20
21
22
23
24

25 In order to calculate the electrophoretic mobility of the analyte molecules, the residence time
26 of the analyte molecules was calculated using
27

$$28 \quad t = \frac{l A}{Q}$$

29
30
31

32 where l length of the electrodes, Q is the volumetric flow rate, and A is the cross sectional area of the
33 electrophoresis channel perpendicular to the electrodes. The deflection in the electrophoresis
34 chamber was then calculated from the images of the analyte molecules deflected in the channels. The
35 profiles of the fluorescent beam of deflected analyte molecules was plotted for each image taken at
36 each voltage step, and the mean deflection of each profile recorded at each step. The electrophoretic
37 mobility μ of an analyte molecule was calculated by
38
39
40
41
42

$$43 \quad \mu = \frac{v}{E_{\text{eff}}}$$

44
45

46 where v is the migration velocity (mean distance deflected divided by the residence time) and E_{eff} is
47 the effective electric field across the electrophoresis channel. Therefore, a plot of v vs E_{eff} yields a
48 slope of μ .
49
50

51 The effective electric field across the device, equivalent to V_{eff}/d , was obtained through
52 calibration of each device. The voltage drop across the electrode channels on both sides was
53 calculated using $R_{\text{electrodes}} = V/I$ by measuring the current through the device at each applied voltage
54 in the calibration. We then compared this to the electrical resistance of the entire device filled with
55
56
57
58
59
60

1
2
3 buffer, obtained in the measurements through $R_{\text{device}} = V / I$. Therefore, we calculated the resistance
4 of the main channel as $R_{\text{main}} = R_{\text{device}} - R_{\text{electrodes}}$, and thereby the voltage drop across the main channel.
5 (Reference Saar paper) The voltage drop across the main channel can also be expressed as a
6 percentage drop relative to the applied voltage by taking the ratio of $R_{\text{electrodes}}/R_{\text{device}}$, and typically,
7 we obtained voltage efficiencies varying from 4 % to 12 %. This allowed E_{eff} to be determined and
8 therefore the mobility μ of the analyte to be calculated.
9
10
11
12

13 The measured electrophoretic mobilities were converted to solvated charges for each protein.
14 At equilibrium at each applied voltage, the electrical force exerted on the analyte molecules balance
15 with the drag force arising from analyte migration through the solution. Given this condition, the
16 charge to radius ratio for a spherical analyte molecule can be expressed as
17
18
19
20

$$\frac{q}{r} = 6\pi\eta\mu$$

21 where η is the viscosity of solution⁴⁶.
22
23
24
25
26

27 Profiles analysis

28
29 The profiles were analysed by OriginPRO software. Smoothing was realised applying in series a
30 parabolic low pass FFT and a Savitzky-Golay filter (2nd order, 21 pt). Then, the second derivative of
31 the smoothed signal was calculated and it was considered a peak any signal above the noise, which
32 was defined as the root mean square of the signal on the channel and outside of the electrophoretic
33 profile (**Figure 7a**). The convolution fits converged with a chi-squared tolerance of $1 \cdot 10^{-6}$ (**Figure**
34 **4b** and **Figure 7d**).
35
36
37
38
39
40

41 Microfluidic diffusion measurements

42
43 Bonded microfluidic diffusion devices were filled with buffer from the outlet with either a
44 500 μL or 1 mL gastight glass syringe (Hamilton) connected to a needle (Neolus Terumo, 25 gauge,
45 0.5 x 16 mm) and polythene tubing (Fischer scientific, inner diameter 0.38 mm, outer diameter 1.09
46 mm). The inlets were loaded with buffer and sample using gel-loading pipette tips. The syringe was
47 then attached to a neMESYS pump (Centoni), which allowed accurate and precise control of the fluid
48 flow rate through the channels. The fluid withdrawal rate was set between 160 to 300 $\mu\text{L}/\text{h}$, and the
49 device left to equilibrate for 15 minutes. The channels were then imaged at the nozzle and at 12
50 positions along the diffusion channels (at 0.3, 0.5, 0.9, 1.0, 1.9, 2.0, 2.9, 3.0, 5.9, 6.0, 8.9, and 9 cm
51 from the nozzle) using a UV intrinsic fluorescence microscope described previously.²⁴ Exposure
52
53
54
55
56
57
58
59
60

1
2
3 times ranged from 1000 to 3000 ms depending on the fluorescence intensity of the sample under
4 observation. Fitting of the basis functions to the experimental data was performed as described
5 previously.²⁶ The basis functions used in the analysis were simulated in the range of radii relevant to
6 the samples, normally varying from 0.25 nm to 10 nm in increments of 0.25 nm or 0.5 nm.⁴⁷
7
8
9

10 11 **Acknowledgement**

12
13
14
15 We thank Swiss National Fondation for Science (SNF) for the financial support (grant number
16 P2ELP2_162116 and P300P2_171219). The research leading to these results has received funding
17 from the European Research Council under the European Union's Seventh Framework Programme
18 (FP7/2007-2013) through the ERC grant PhysProt (agreement n° 337969) and from the European
19 Union's Horizon 2020 research and innovation programme under ETN grant 674979-NANOTRANS.
20 We also thank the Engineering and Physical Sciences Research Council for their financial support.
21
22
23
24
25

26 27 **Supporting Information Available**

28
29 This material is available free of charge via the Internet at <http://pubs.acs.org/>.
30
31

32 33 **Notes**

34
35 The authors declare the following competing financial interest(s): Part of the work described in this
36 paper was undertaken as a collaboration with Fluidic Analytics Ltd., of which M.A.W. is a current
37 employee and T.P.J.K. is a board member.
38
39
40
41
42
43
44
45
46
47
48
49
50
51
52
53
54
55
56
57
58
59
60

References

- 1 Djabali, K., de Néchaud, B., Landon, F. & Portier, M. M. AlphaB-crystallin interacts with intermediate filaments in response to stress. *J. Cell Sci.* **110**, 2759-2769, (1997).
- 2 Muchowski, P. J. Protein misfolding, amyloid formation, and neurodegeneration: a critical role for molecular chaperones? *Neuron* **35**, 9-12, (2002).
- 3 Rekas, A. et al. Interaction of the molecular chaperone alphaB-crystallin with alpha-synuclein: effects on amyloid fibril formation and chaperone activity. *J. Mol. Biol.* **340**, 1167-1183, (2004).
- 4 Rekas, A., Jankova, L., Thorn, D. C., Cappai, R. & Carver, J. A. Monitoring the prevention of amyloid fibril formation by alpha-crystallin. Temperature dependence and the nature of the aggregating species. *FEBS J.* **274**, 6290-6304, (2007).
- 5 Waudby, C. A. et al. The interaction of alphaB-crystallin with mature alpha-synuclein amyloid fibrils inhibits their elongation. *Biophys. J.* **98**, 843-851, (2010).
- 6 Shammas, S. L. et al. Binding of the Molecular Chaperone α B-Crystallin to A β Amyloid Fibrils Inhibits Fibril Elongation. *Biophys. J.* **101**, 1681-1689, (2011).
- 7 Raman, B. et al. AlphaB-crystallin, a small heat-shock protein, prevents the amyloid fibril growth of an amyloid beta-peptide and beta2-microglobulin. *Biochem. J.* **392**, 573-581, (2005).
- 8 Knowles, T. P. et al. Kinetics and thermodynamics of amyloid formation from direct measurements of fluctuations in fibril mass. *Proceedings of the National Academy of Sciences* **104**, 10016-10021, (2007).
- 9 Baldwin, A. J., Lioe, H., Robinson, C. V., Kay, L. E. & Benesch, J. L. alphaB-crystallin polydispersity is a consequence of unbiased quaternary dynamics. *J Mol Biol* **413**, 297-309, (2011).
- 10 Aquilina, J. A., Benesch, J. L. P., Bateman, O. A., Slingsby, C. & Robinson, C. V. Polydispersity of a mammalian chaperone: mass spectrometry reveals the population of oligomers in alphaB-crystallin. *Proc. Natl. Acad. Sci. U. S. A.* **100**, 10611-10616, (2003).
- 11 Haley, D. A., Horwitz, J. & Stewart, P. L. The small heat-shock protein, alphaB-crystallin, has a variable quaternary structure. *J. Mol. Biol.* **277**, 27-35, (1998).
- 12 Bagn eris, C. et al. Crystal structures of alpha-crystallin domain dimers of alphaB-crystallin and Hsp20. *J. Mol. Biol.* **392**, 1242-1252, (2009).
- 13 Baldwin, A. J. et al. The polydispersity of α B-crystallin is rationalized by an interconverting polyhedral architecture. *Structure* **19**, 1855-1863, (2011).
- 14 Jehle, S. et al. Solid-state NMR and SAXS studies provide a structural basis for the activation of alphaB-crystallin oligomers. *Nat. Struct. Mol. Biol.* **17**, 1037-1042, (2010).
- 15 Hochberg, G. K. A. & Benesch, J. L. P. Dynamical structure of α B-crystallin. *Progress in biophysics and molecular biology*, (2014).
- 16 Jehle, S. et al. alphaB-crystallin: a hybrid solid-state/solution-state NMR investigation reveals structural aspects of the heterogeneous oligomer. *J. Mol. Biol.* **385**, 1481-1497, (2009).
- 17 Laganowsky, A. et al. Crystal structures of truncated alphaA and alphaB crystallins reveal structural mechanisms of polydispersity important for eye lens function. *Protein Sci.* **19**, 1031-1043, (2010).
- 18 Delbecq, S. P., Jehle, S. & Klevit, R. Binding determinants of the small heat shock protein, α B-crystallin: recognition of the 'IxI' motif. *EMBO J.* **31**, 4587-4594, (2012).

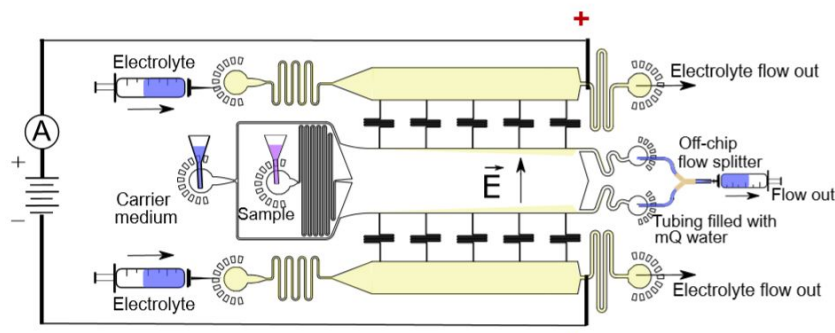
- 1
2
3 19 Baldwin, A. J. et al. Quaternary dynamics of α B-crystallin as a direct consequence
4 of localised tertiary fluctuations in the C-terminus. *J. Mol. Biol.* **413**, 310-320, (2011).
5 20 Hochberg, G. K. A. et al. The structured core domain of α B-crystallin can prevent
6 amyloid fibrillation and associated toxicity. *Proc. Natl. Acad. Sci. U. S. A.* **111**, E1562--
7 1570, (2014).
8 21 Ecroyd, H. & Carver, J. A. Crystallin proteins and amyloid fibrils. *Cell. Mol. Life Sci.*
9 **66**, 62-81, (2009).
10 22 Carver, J. A., Aquilina, J. A., Truscott, R. J. & Ralston, G. B. Identification by ¹H NMR
11 spectroscopy of flexible C-terminal extensions in bovine lens alpha-crystallin. *FEBS*
12 *Lett.* **311**, 143-149, (1992).
13 23 Saar, K. L. et al. On-chip label-free protein analysis with downstream electrodes for
14 direct removal of electrolysis products. *Lab Chip* **18**, 162-170, (2018).
15 24 Challa, P. K. et al. Real-Time Intrinsic Fluorescence Visualization and Sizing of
16 Proteins and Protein Complexes in Microfluidic Devices. *Analytical Chemistry* **90**,
17 3849-3855, (2018).
18 25 Artimo, P. et al. ExPASy: SIB bioinformatics resource portal. *Nucleic Acids Research*
19 **40**, W597--W603, (2012).
20 26 Arosio, P. et al. Microfluidic diffusion analysis of the sizes and interactions of proteins
21 under native solution conditions. *ACS nano* **10**, 333-341, (2015).
22 27 Erickson, H. P. Size and Shape of Protein Molecules at the Nanometer Level
23 Determined by Sedimentation, Gel Filtration, and Electron Microscopy. *Biological*
24 *Procedures Online* **11**, 32-51, (2009).
25 28 Pace, C. N., Grimsley, G. R. & Scholtz, J. M. Protein Ionizable Groups: pK Values and
26 Their Contribution to Protein Stability and Solubility. *Journal of Biological*
27 *Chemistry* **284**, 13285-13289, (2009).
28 29 Damodaran, S., Parkin, K. & Fennema, O. *Fennemas Food Chemistry, Amino Acids,*
29 *Peptides and Proteins.* (2008).
30 30 Ruggeri, F. S. et al. Identification of Oxidative Stress in Red Blood Cells with
31 Nanoscale Chemical Resolution by Infrared Nanospectroscopy. *Int J Mol Sci* **19**,
32 2582, (2018).
33 31 Ruggeri, F. S. et al. Nanoscale studies link amyloid maturity with polyglutamine
34 diseases onset. *Sci Rep* **6**, 31155, (2016).
35 32 Qamar, S. et al. FUS Phase Separation Is Modulated by a Molecular Chaperone and
36 Methylation of Arginine Cation- π Interactions. *Cell* **173**, 720-734 e715, (2018).
37 33 Li, Z. et al. Solution fibre spinning technique for the fabrication of tuneable
38 decellularised matrix-laden fibres and fibrous micromembranes. *Acta Biomater* **78**,
39 111-122, (2018).
40 34 Muller, T. et al. Nanoscale spatially resolved infrared spectra from single
41 microdroplets. *Lab Chip* **14**, 1315-1319, (2014).
42 35 Shimanovich, U. et al. Silk micrococoon for protein stabilisation and molecular
43 encapsulation. *Nat Commun* **8**, 15902, (2017).
44 36 Volpatti, L. R. et al. Micro- and nanoscale hierarchical structure of core-shell protein
45 microgels. *Journal of Materials Chemistry B* **4**, 7989-7999, (2016).
46 37 Lapinska, U. et al. Gradient-free determination of isoelectric points of proteins on
47 chip. *Phys. Chem. Chem. Phys.* **19**, 23060-23067, (2017).
48 38 Frigon, R. P., Leyboldt, J. K., Uyeji, S. & Henderson, L. W. Disparity between Stokes
49 radii of dextrans and proteins as determined by retention volume in gel permeation
50 chromatography. *Analytical Chemistry* **55**, 1349-1354, (1983).
51 39 Susi, H. & Byler, D. M. Protein structure by Fourier transform infrared spectroscopy:

- 1
2
3 Second derivative spectra. *Biochemical and Biophysical Research Communications*
4 **115**, 391-397, (1983).
- 5 40 Susi, H. & Byler, D. M. in *Enzyme Structure Part K Vol. 130* 290-311 (Academic
6 Press, 1986).
- 7 41 Ruggeri, F. S. et al. Infrared nanospectroscopy characterization of oligomeric and
8 fibrillar aggregates during amyloid formation. *Nat Commun* **6**, 7831, (2015).
- 9 42 Qin, D., Xia, Y. & Whitesides, G. M. Soft lithography for micro- and nanoscale
10 patterning. *Nat. Protoc.* **5**, 491-502, (2010).
- 11 43 Challa, P. K., Kartanas, T., Charmet, J. & Knowles, T. P. Microfluidic devices
12 fabricated using fast wafer-scale LED-lithography patterning. *Biomicrofluidics* **11**,
13 014113, (2017).
- 14 44 Tan, S. H., Nguyen, N. T., Chua, Y. C. & Kang, T. G. Oxygen plasma treatment for
15 reducing hydrophobicity of a sealed polydimethylsiloxane microchannel.
16 *Biomicrofluidics* **4**, 1-8, (2010).
- 17 45 Bodas, D. & Khan-Malek, C. Hydrophilization and hydrophobic recovery of PDMS by
18 oxygen plasma and chemical treatment—An SEM investigation. *Sensors and*
19 *Actuators B: Chemical* **123**, 368-373, (2007).
- 20 46 Herling, T. et al. Integration and characterization of solid wall electrodes in
21 microfluidic devices fabricated in a single photolithography step. *Applied Physics*
22 *Letters* **102**, 184102, (2013).
- 23 47 Müller, T. et al. in *International Journal of Nonlinear Sciences and Numerical*
24 *Simulation Vol. 17* 175 (2016).
- 25
26
27
28
29
30
31
32
33
34
35
36
37
38
39
40
41
42
43
44
45
46
47
48
49
50
51
52
53
54
55
56
57
58
59
60

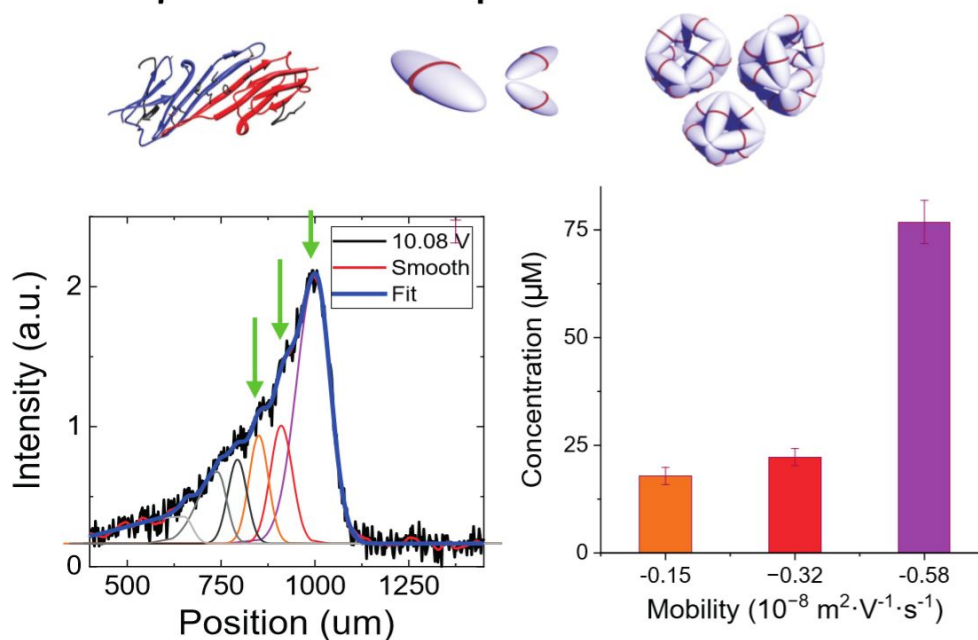
Table of Contents Entry

Insights into α B-crystallin polydispersity from native microfluidic high-field electrophoresis measurements

(a) High-field electrophoresis



(b) Separation and characterisation of protein complexes



Microfluidic high-field electrophoresis and diffusional sizing provide insights into the oligomerisation of the molecular chaperone α B-crystallin.